TÜBİTAK

Turkish Journal of Physics

http://journals.tubitak.gov.tr/physics/

Research Article

Turk J Phys
(2015) 39

doi:10.3906/fiz-1412-7

Synthesis and properties of a spinel cathode material for lithium ion battery with flat potential plateau

Ahmed Abdulrahman Ahmed AL-TABBAKH[1,*], Norlida KAMARULZAMAN[2], Aseel Basim AL-ZUBAIDI[3]

[1]Department of Physics, Al-Nahrain University, Jadiriya, Baghdad, Iraq
[2]Centre for Nanomaterials Research, Institute of Science, Universiti Teknologi MARA, Shah Alam, Selangor, Malaysia
[3]Department of Materials Engineering, University of Technology, Baghdad, Iraq

Received: 18.12.2014 • **Accepted/Published Online:** 03.04.2015 • **Printed:** 30.07.2015

Abstract: A potential cathode material for lithium ion battery was synthesised by combustion reaction. The thermal behaviour of the as-synthesised precursor was measured using a thermogravimetric analyser and the range of calcination temperature from 500 °C to 800 °C was determined. X-ray diffraction analysis showed that all calcined powders crystallised in the cubic spinel structure of the $Fd\bar{3}m$ space group. The particle size distributions and morphologies of the powders were obtained using a particle size analyser and scanning electron microscope. The effect of calcination temperature on the electrochemical performance was investigated using galvanostatic charge/discharge measurements. The potential profiles of charge and discharge exhibited flat plateaus, emphasising that the synthesised batteries are not super capacitors. Results showed that the batteries prepared from powders calcined at 800 °C exhibited higher coulombic efficiency and better cycling performance than powders calcined at 500 °C.

Key words: Li-ion batteries, transition-metal compounds, combustion synthesis, electrochemical properties, X-ray diffraction

1. Introduction

The profile of the charge/discharge potential curve with capacitor-like behaviour is one major weakness observed in lithium ion batteries. The capacitor-like behaviour is the linear variation of the battery potential in accordance with the intercalation/deintercalation of lithium ions into/from the active material. It is attributed to the low electronic conductivity and low lithium ion diffusion coefficient of the active material and is most likely to increase with the plateau voltage and the charge/discharge currents [1]. The usefulness of the battery material for industrial and technological purposes depends largely on moderating this problem. Lithiated transition metal oxides of spinel structures have been recognised as potential cathode materials for high energy and high power density lithium secondary batteries due to high conductivity and high lithium diffusion coefficient [2–4]. Cathode materials containing manganese and nickel in the form of $LiNi_xMn_{2-x}O_4$ have been extensively investigated due to their high operating potentials, lower toxicity than cobalt-containing cathodes, and low cost [5,6]. However, increasing the nickel content of the cathode material invites disadvantages like formation of impurities during synthesis and fast capacity fade at elevated temperatures [7,8]. Partial substitution of either or both of the aforementioned transition metals with other cations like Fe is thought to overcome these

*Correspondence: tabbakh2003@yahoo.com

disadvantages and improve the electrochemical performances of the cathodes [9]. However, the high voltage potential of these materials is always accompanied by noticeable potential drop across the high potential plateaus. In this work we report the synthesis, characterisation, and properties of a spinel cathode material of the form $Li_{1.03}Mn_{1.72}Ni_{0.16}Fe_{0.04}O_4$ having a flat potential plateau with minimal potential drop. The effect of calcination temperature on the electrochemical performance of the material was investigated using galvanostatic charge/discharge measurements. The results reported in the present discussion suggest that the present material is a potential candidate for lithium rechargeable batteries for high power density applications.

2. Experimental work

2.1. Synthesis and characterisation of the material

Synthesis of the cathode material was achieved by a self-propagating combustion reaction [10,11]. Stoichiometric amounts of $LiNO_3$, $Mn(NO_3)_2.4H_2O$, $Ni(NO_3)_2.6H_2O$, and $Fe(NO_3)_3.9H_2O$ were dissolved in deionised water at room temperature. The solution was then kept on magnetic stirring for 3 h to confirm dissolution of the nitrates. An aqueous solution of citric acid ($C_6H_8O_7$), used as fuel for the combustion reaction, was added to the homogenised mixture at 100 °C. Fuel amount was determined from the oxidation to reduction ratio of the reactants. Prior to the combustion, excess water was evaporated from the solution at a moderate temperature (below 150 °C) until a dense solution was obtained. The temperature of the solution was finally raised at a high rate to the combustion temperature to prevent formation of impurities [12]. The combustion reaction was a smouldering (flameless) type and self-propagating, resulting in a fine powdered precursor. Figure 1 shows the phases of the synthesis reaction just before the combustion (i.e. Figure 1a), during combustion (Figure 1b), and just after the combustion took place (Figure 1c). In Figure 1b it is clear that combustion took place consistently throughout the reaction vessel.

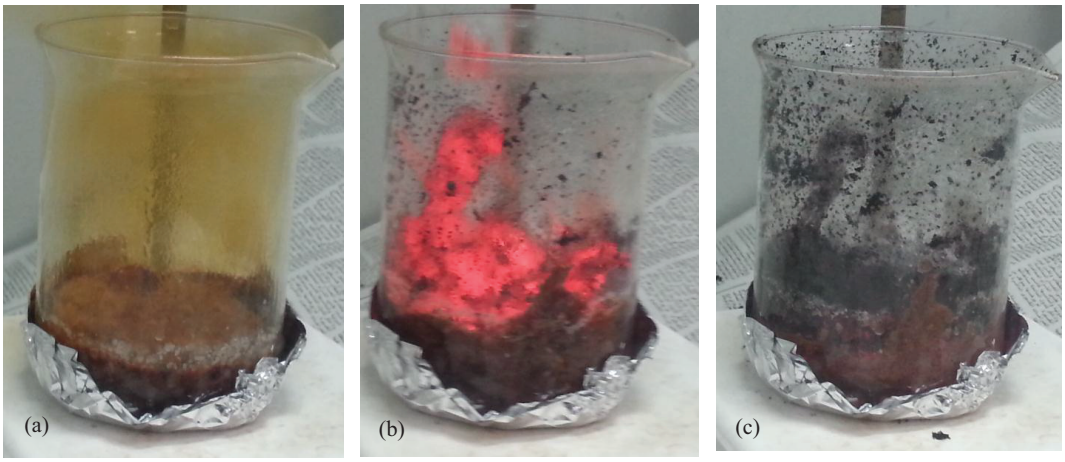

Figure 1. The phases of the combustion reaction: **(a)** formation of frothed solution of the reactants, **(b)** instant of combustion, and **(c)** formation of precursor just after combustion of the reactants.

The produced precursor from the reaction was thermally analysed using a high-performance modular thermogravimetric SETSYS Evolution Analyser from SETARAM Instrumentation to estimate the best calcination temperature. A few milligrams of the precursor were loaded on the analyser crucible. Thermogravimetric (TG) and heat flow graphs were obtained at a 10 °C/min heating rate under the flow of a protective gas.

Calcination of the precursors was achieved by admitting the precursor powder into a hot furnace at a pre-set temperature to prevent formation of oxide impurities and to produce pure powders [12]. The calcined powders were then processed by a high-energy ball mill operated at 600 rpm using 9 balls of 4 g each to produce finer powders. It is well known that size reduction of the material particles may enhance the material's attainable capacity and rate capability due to increase of surface to volume ratio [13].

The powders were then characterised by particle size distribution and X-ray diffraction (XRD) measurements. The size distributions were measured using a Malvern Mastersizer Range particle size analyser from Malvern Instruments [14]. Precise amounts of the powders were dispersed in distilled water and sonicated for 15 min to achieve the required dispersion of the particles. Measurements were repeated several times to ensure consistency of results. The XRD measurements were carried out with a PANalytical X'pert Pro MDP instrument with a real-time multiple strip type solid-state detector (known as the X'celerator), spinner holder, and Bragg–Brentano reflection-parafocusing geometry. The morphologies of the powders were examined using a JSM-6700F field emission scanning electron microscope (SEM) from JEOL. A few randomly selected specimens were investigated under similar working conditions and high magnification.

2.2. Cathode fabrication, battery assembly, and test

Slurries were formed and homogenised from a mixture of 0.025 g of the active material, 0.003 g of activated carbon, 0.0027 g of polyvinylidene fluoride (PVDF) binder, and a few droplets of acetone. These slurries were then pasted on metallic mesh serving as current collectors. The fabricated cathodes were dried at 200 °C for 24 h before being admitted to the batteries' fabrication chamber. The lithium ion batteries were assembled in Teflon battery holders inside a glove-box from Unilab Analyse under a dry argon atmosphere. The assembled cells were composed of the fabricated cathodes as the positive electrode, a porous polypropylene separator (Celgard 2500), and a Li foil anode, all immersed in 1 M lithium hexaflurophosphate $LiPF_6$ electrolyte in a 1:1 volume ratio of ethylene carbonate and dimethyl carbonate. Each electrode had dimensions of (1×1) cm^2. The charge and discharge equilibrium potential profiles were measured in the voltage ranges from open-circuit voltage to 4.2 V and from 4.2 V to 1.0 V. The charge and discharge currents were fixed at 0.5 mA (20 mA/g). The assembled batteries were operated for 20 cycles of charge and discharge at a constant current of 1 mA using a 16-channel automatic battery cycler WBCS3000 from WonATech. Specific capacity values were determined from the applied current, time of discharge, and active material loading in the cathodes (i.e. 0.025 g). Measurements were achieved at room temperature and repeated several times to ensure reproducibility of results.

3. Results and discussion

The reaction is proposed to take place in three ideal steps, as shown schematically in Figure 2. In the first step the metal nitrates react with water-producing metals, hydroxides, and nitric acid. The second step, where the citric acid added, results in the formation of intermediate compounds of the metal carboxyl. The carboxyls are expected to react with the HNO_3 (formed in the first step) during the combustion of the mixture and produce the final precursor, which is composed of the lithiated metal oxide (i.e. $Li_{1.03}Mn_{1.72}Ni_{0.16}Fe_{0.04}O_4$), carbon monoxide, nitrogen, and water. The three steps mentioned above are meant to take place in the ideal and complete reaction, which is practically difficult to achieve. Therefore, some impurities of other compounds may form during the synthesis procedure. $FeMnO_3$ is one such impurity that has been identified from the XRD patterns of the as-synthesised powders. This will be further discussed in the following paragraphs. Formation of this impurity is expected to take place during the last step, where FeHCOOH reacts with MnHCOOH in

the presence of nitric acid according to the formula (i.e. $FeHCOOH + MnHCOOH + 2HNO_3 \rightarrow FeMnO_3 + 3H_2O + 2CO_2 + N_2$). Formation of Fe_2O_3 is also possible as the temperature is raised above 200 °C and just before the combustion of the mixture occurs. Nevertheless, Fe_2O_3 may react with the citric acid producing FeHCOOH in the second step of the reaction in what is thought to be a self-correcting step (referred to with the vertical dashed arrows in Figure 2). It is therefore thought that raising the temperature of the nitrates' aqueous solution in the first step of the reaction (before adding $C_6H_8O_7$ to the mixture) should not exceed the formation temperature of the Fe_2O_3. Other hydrocarbon impurities (e.g., LiC_3, LiC_4, LiC_6, and Li_2C_2) may also form in the second step of the reaction, as shown in Figure 2 (horizontal dashed arrow). These are expected to react with HNO_3 to produce lithium hydroxide, which ultimately takes part in the third step of the reaction (i.e. the combustion of the materials) [10,11,15].

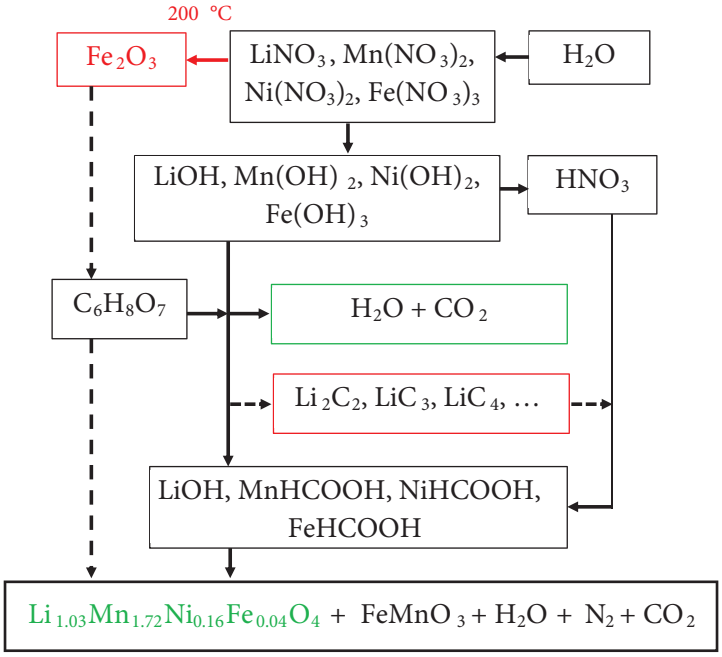

Figure 2. The proposed reaction route for the synthesis of the cathode material by combustion method. The dashed arrows indicate incomplete combustion and formation of impurity phases.

The TG and associate heat flow curves are shown in Figure 3. The TG curve exhibits four distinct regions of mass losses as indicated by m_1 through m_5 in Figure 3. Based on the temperatures ranges and the nature of the heat flow curve, the first region (m_1–m_2) was attributed to loss of water. The second region (m_2–m_3) is due to decomposition of some residual hydrocarbons that might not have taken part in the reaction. The third region (from m_3 to m_4) was attributed to decomposition of $FeMnO_3$ and formation of the pure phase of spinel $Li_{1.03}Mn_{1.72}Ni_{0.16}Fe_{0.04}O_4$ compound. The mass loss in the last region (m_5) could only be attributed to delithiation of the spinel $Li_{1.03}Mn_{1.72}Ni_{0.16}Fe_{0.04}O_4$ by lithium evaporation. Mass losses, corresponding masses, and molar masses of each region are presented in Table 1.

This analysis suggests that the as-synthesised precursor was composed of 94.5% $Li_{1.03}Mn_{1.72}Ni_{0.16}Fe_{0.04}O_4$, 2.2% $FeMnO_3$, 1.7% hydrocarbons, and 1.6% residual water vapour. Based on the TG analysis the as-synthesised precursor was divided into two quantities, one of which was calcined at 500 °C for 24 h and the other at 800 °C for 24 h. Both powders were then subjected to ball milling to produce fine powders labelled hereafter

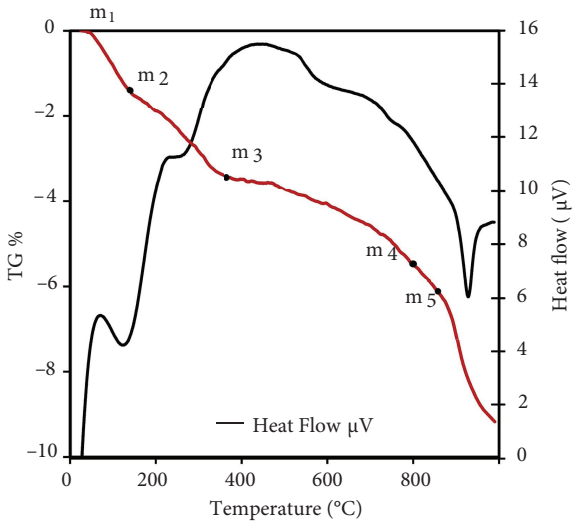

Figure 3. TG and associate heat flow curves of the thermally analysed precursor. Masses and corresponding molecular masses at m_1: 14 mg, 187.582 g/mol. m_2: 13.776 mg, 184.581 g/mol. m_3: 13.538 mg, 181.392 g/mol. m_4: 13.23 mg, 177.265 g/mol. m_5: 13.104 mg, 175.577 g/mol.

Table 1. Mass losses, molar masses, and composition of material at TG curve regions.

Region	T (°C)	Mass (mg)	Molar mass (g/mol)	Mass loss (mg)	Composition
m1	25	14.00	187.582	0.0	$1Li_{1.03}Mn_{1.72}Ni_{0.16}Fe_{0.04}O_4$ + $0.16747H_2O$ + 0.0503(hydrocarbons) + $0.026FeMnO_3$
m2	166	13.775	184.581	0.224	$Li_{1.03}Mn_{1.72}Ni_{0.16}Fe_{0.04}O_4$ + $0.026FeMnO_3$ + 0.0503(hydrocarbons)
m3	340	13.538	181.392	0.238	$Li_{1.03}Mn_{1.72}Ni_{0.16}Fe_{0.04}O_4$ + $0.026FeMnO_3$
m4	800	13.230	177.265	0.308	$Li_{1.03}Mn_{1.72}Ni_{0.16}Fe_{0.04}O_4$ *
m5	875	13.104	175.577	0.126	$Li_{0.8}Mn_{1.72}Ni_{0.16}Fe_{0.04}O_4$

*Pure phase identified from XRD patterns.

as P500 and P800 powders. The size distribution measurements are presented in Figures 4a and 4b. The size distribution of the P500 powder (Figure 4a) exhibits a single population with an average size of 262 nm. The size distribution from the P800 powder (Figure 4b) exhibits two populations near 220 nm and 2669 nm with an average size of 274 nm. Comparison of the two distributions shows that raising the calcination temperature to 800 °C leads to formation of larger particles as the degree of crystallinity increases with the rising temperature. The lower size population of the P800 powder is thought to arise from the fragments of the larger particles due to the milling process. The powders' morphologies, examined under SEM, are shown in the SEM images of Figures 5a and 5b for the P500 and P800 powders, respectively. It is clear from the two SEM images that P800 exhibits larger particles than P500. The P800 powder is less populated with small particles that are produced from the milling effect than the P500 powder. Particle geometries of the P800 powder are also closer to the octahedral shape of the spinel structure where milling conditions are less effective on highly crystalline particles. Particles sizes were measured from the SEM images as shown by the arrows on each image. The sizes

obtained from the SEM measurements were lower than those obtained from the particle size analyser. This is justified by the fact that the size measurements using the particle size analyser are diffraction-limited, whereas such limitations using electrons are insignificant in the SEM measurements [14]. Furthermore, aggregation of particles may result in higher size measurements using the particle size analyser.

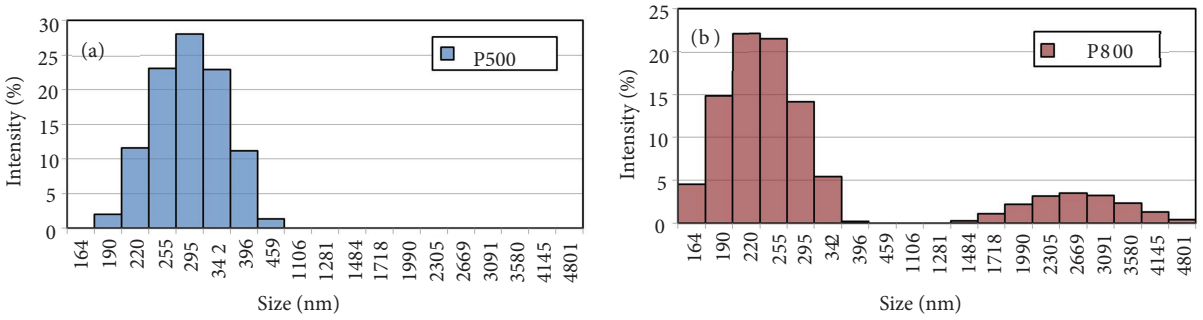

Figure 4. The particle size distributions obtained for the calcined powders: (a) calcination at 500 °C, (b) calcination at 800 °C. All powders were subjected to high-energy ball milling prior to measurements.

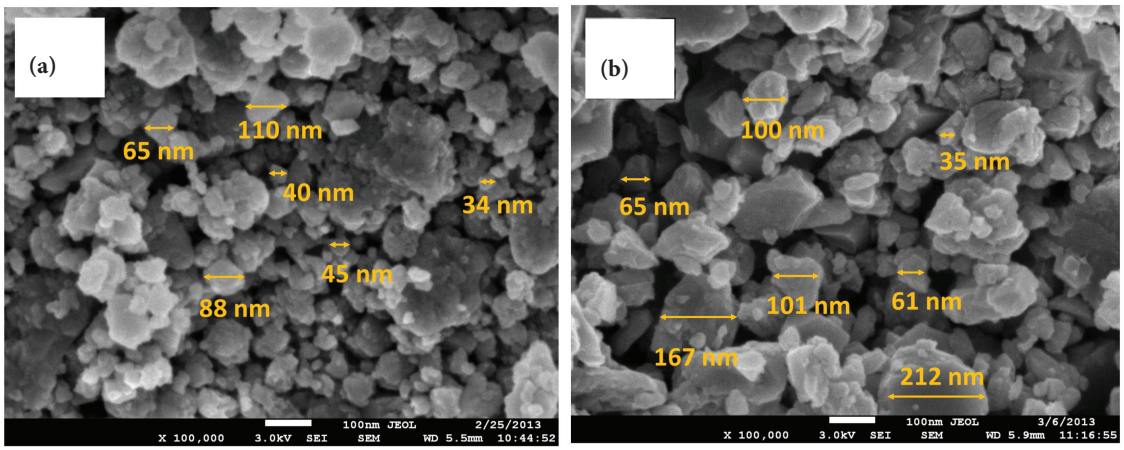

Figure 5. Morphologies of powders as shown under scanning electron microscope: (a) powder calcined at 500 °C, (b) powder calcined at 800 °C.

The XRD patterns of the two powders are presented in Figure 6. Peaks of high intensities were obtained for both powders using the solid-state detector with a reasonable step-time. The high intensity peaks indicate that highly crystalline powders were produced successfully by subjecting powders to the calcination conditions (i.e. 500 °C or higher for 24 h). Intensities were found to increase with the rising of calcination temperature, whereas the full-width at half-maximum (FWHM) of the main reflections decreased. Comparison of peaks heights and FWHM are presented in Table 2. This shows that increasing the calcination temperature improved the crystalline quality of the synthesised powders [16].

For the P800 powder, these peaks could be indexed to a single-phase of cubic spinel structure with space group $Fd\bar{3}m$ (space group number 227) of lithium manganese oxide (ICSD 088138) [17]. No significant peaks could be assigned to the impurity phase in the calcined powder. Unlike P800, the XRD patterns of P500 showed impurity peaks. The XRD patterns could be indexed with reference to two phases of a cubic spinel structure (space group $Fd\bar{3}m$) of lithium manganese oxide (ICSD 090132) and a cubic structure (space group

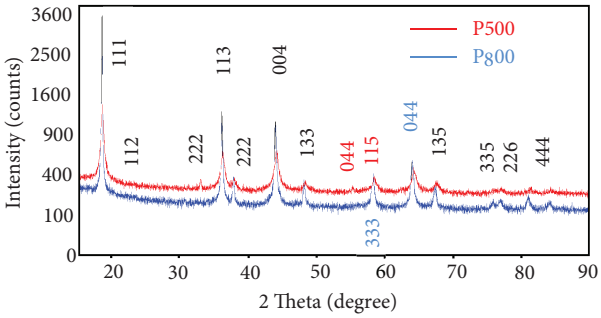

Figure 6. Comparison of XRD patterns of the P500 and P800 powders. Peaks indexed in black are common between the two patterns.

Table 2. Peak parameters of main reflections of XRD patterns obtained from P500 and P800 powders.

	Intensity (counts)			FWHM (°2θ)		
Peak	(111)	(113)	(004)	(111)	(113)	(004)
P500	1158	424	467	0.44	0.56	0.65
P800	3734	1095	1040	0.17	0.28	0.33

$Ia\bar{3}$) of $FeMnO_3$ (ICSD 1011266) [18,19]. XRD data analysis and Rietveld refinement suggested that P500 was composed of 97% $Li_{1.03}Mn_{1.72}Ni_{0.16}Fe_{0.04}O_4$ and 3% $FeMnO_3$ as estimated from the intensity ratio of these two phases (see Figures 7a–7c). This was found to agree with the TG analysis of the as-synthesised precursors (i.e. 2.2% for the $FeMnO_3$ phase), which was increased to about 2.8% after discarding residual water and hydrocarbon impurities. The structural and stoichiometric parameters for the two powders obtained from the refinement of the XRD patterns are presented in Tables 3 and 4.

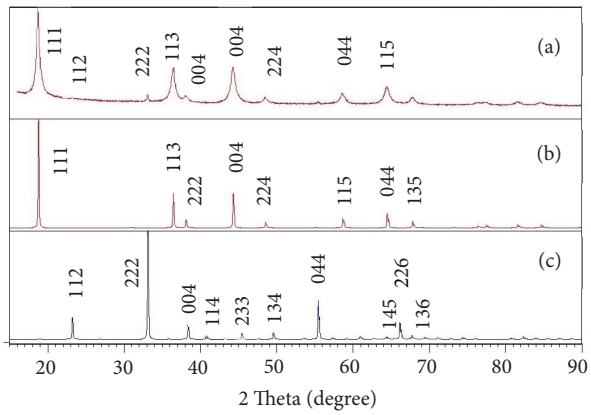

Figure 7. Indexing of the main reflections of the XRD spectrum (spectrum (a)) obtained from the P500 powder to $Fd\bar{3}m$ spinel phase (i.e. (b) ICSD: 090132, Fd-3m, $LiMn_2O_4$) and $Ia\bar{3}$ cubic phase (i.e. **(c)** ICSD:1011266, Ia-3, $FeMnO_3$).

The ionic distribution and the corresponding occupancies are shown in the same tables, where Mn, Ni, and Fe ions occupy the octahedral 16d sites of the spinel structure with occupancies appropriate to the stoichiometric composition of the spinel phase. Li ions occupy the tetrahedral 8a sites in addition to a fractional occupancy at the octahedral 16d sites. The oxygen ions reside at the 32e sites of the unit cell forming the three-dimensional frame of the spinel structure. This is in agreement with the reported results of the spinel structure, which has a

Table 3. Structural and stoichiometric parameters of the P800 powder.

Formula of refined structure			a (nm)		Density (g/cm^3)	R_{wp}%	GOF
$Li_{1.03}Mn_{1.719}Ni_{0.159}$ $Fe_{0.04}O_{3.98}$			0.820254(9)		4.245(4)	4.222	1.1443
Space group (no.) and structure			$Fd\bar{3}m$ (1) cubic				
Atom	Wyckoff's	SOF	X	Y	Z	B(iso.)	
Li-a	8a	1.000	0.125	0.125	0.125	0.5439	
Li-b	16d	0.0149	0.500	0.500	0.500	0.5877	
Mn	16d	0.8596	0.500	0.500	0.500	0.4561	
Ni	16d	0.0798	0.500	0.500	0.500	0.4760	
Fe	16d	0.0200	0.500	0.500	0.500	0.5211	
O	32e	0.9958	0.25899	0.25899	0.25899	0.9083	

Table 4. Structural and stoichiometric parameters of the P500 powder.

Formula	Weight fraction	Space-group no. and structure	a (nm)	Density (g/cm^3)	R_{wp}%	GOF
$Li_{1.0298}Mn_{1.717}Ni_{0.158}Fe_{0.0396}O_{3.943}$	97%	$la\ \bar{3}$m (227) cubic	0.817837	4.3035	2.2554	1.0382

Atom	Wyckoff's	SOF	X	Y	Z	B (iso.)
Li-a	8a	1.000	0.125	0.125	0.125	0.51104
Li-b	16d	0.0149	0.500	0.500	0.500	0.52231
Mn	16d	0.8586	0.500	0.500	0.500	0.38484
Ni	16d	0.0793	0.500	0.500	0.500	0.43297
Fe	16d	0.0198	0.500	0.500	0.500	0.58013
O	32e	0.9858	0.261	0.261	0.261	0.77490

Formula	Weight fraction	Space-group no. and structure	a (nm)	Density (g/cm^3)	R_{wp}%	GOF
$FeMnO_3$	3 %	$la\ \bar{3}$ (206) cubic	0.936530	5.1351	2.2554	1.0382

Atom	Wyckoff's	SOF	X	Y	Z	B (iso.)
Fe-a	8a	0.5	0.00	0.00	0.00	0.5
Mn-a	8a	0.5	0.00	0.00	0.00	0.5
Fe-a	24d	0.5	0.28	0.00	0.25	0.5
Mn-b	24d	0.5	0.28	0.00	0.25	0.5
O	48e	1	0.28	0.365	0.13	0.5

unique character such that the manganese ions can easily be replaced with transition metal ions at the octahedral sites [2,20]. The intensity of the 022 line is negligibly small in the XRD pattern, signifying that no transition metal ions occupy the tetrahedral sites in the spinel phase. As additional proof, the ratio of the 004/113 lines showed no evident decrease, which is in agreement with the previously reported studies for spinel structures [3,20,21]. The site occupancy factor (SOF) of Li at the tetrahedral 8a site is full. At the octahedral sites, fractional occupancy of Li ions, substituting some transition metals ions, is still possible. Similar findings have been reported for nonstoichiometric spinel structures [3]. The unit-cell constant, obtained from the refinement

results, shows an increase in value with the increase of calcination temperature. This suggests that formation of the spinel phase is more complete at 800 °C than at 500 °C [22]. Furthermore, inspection of the site occupancy of the constituting ions justifies the increase of the lattice parameter with temperature, as ion SOFs of P800 are generally higher than the SOFs of P500. Increase of lattice parameter with temperature for the spinel structure was reported by Ghanbarnezhad et al. and Yi et al. [23,24]. The potential profiles of the fabricated batteries are shown in Figure 8. The open-circuit voltage decreases from 3.57 V for the P500 powder to 3.13 V for the P800 powder with respect to Li anode potential, as shown in the inset of Figure 8. This could be attributed to the effect of calcination temperature on the completeness of the spinel phase formation.

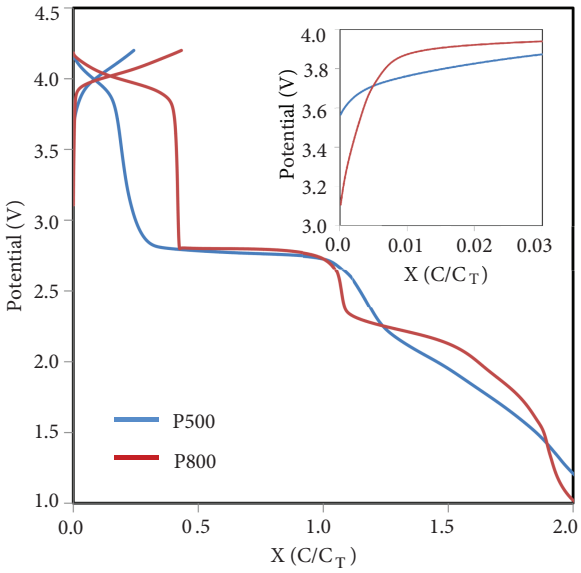

Figure 8. Potential profiles of the lithium ion batteries fabricated from P500 and P800 powders showing typical potential plateaus of spinel structure. Inset: Charge curves at magnified scales showing open circuit potentials of the P500 and P800 batteries.

Both batteries were initially charged to 4.2 V at 1 mA current. Cells were then discharged to 1.0 V at 0.5 mA to determine the equilibrium voltage profile. Above 3 V both cells exhibited a single potential plateau at around 4.0 V, with capacity increases with the increase of calcination temperature. At 3 V potential, the P500 cell delivered 24% of its theoretical capacity, whereas the P800 cell delivered 43% of its theoretical capacity. For further elaboration of this observation, the Li content dependence on the applied voltage was determined from the SOF of Li in the tetrahedral sites of the unit-cell of the cathode active compounds (see Tables 3 and 4). Both powders exhibited similar SOFs of Li, signifying no deficiency in Li occupancy in the tetrahedral sites. However, charging batteries to 4.2 V resulted in extraction of 24% of the Li from the tetrahedral sites of the P500 compound and 43% of the Li from the P800 compound. It seems easier to extract more Li ions from the active material when calcination temperature is higher (i.e. 800 °C). When the batteries discharged the remaining amount of Li in each case has to be taken into consideration while estimating the amount of Li being intercalated back into the active material (i.e. 76% of Li for P500 and 57% for P800). At 2.8 V (onset of the second plateau), the Li content per formula in P500 and P800 was found equal to 1.14 and 0.99, respectively. This implies that while 99% of the extracted lithium was intercalated back into the structure of the P800 cathode compound, overlithiation took place for the P500 compound. Due to further discharge to 2.5 V, the

lithium content was found equal to 1.9 and 1.64 for the P500 and P800 active compounds, respectively, which is determined from the discharge curves of Figure 8 after taking into account the remaining amount of Li content at the cut-off voltage during battery charge. The potentials of the second plateau were found independent of calcination temperature.

It is obvious from the potential profiles of the compounds that while the high-voltage plateau shows a prominent linear variation of potential in accordance with the intercalation of lithium (i.e. a capacitor-like behaviour), the second plateau exhibits a remarkably flat characteristic. For the P800 compound, the voltage drop across the potential plateau is equal to 18.8 mV/h at 40 mA/g current density and increases linearly with the discharge current. The P500 compound exhibits a slightly higher voltage drop across its potential plateau. The capacitor-like behaviour has been attributed to low electronic conductivity and low lithium ion diffusion coefficient [1] and, therefore, the usefulness of the battery material for industrial and the technological purposes depends largely on moderating this problem. Based on that, it is proposed to operate the present batteries in the voltage range of the low potential plateau where such capacitor-like behaviour is insignificant.

The charge and discharge curves of the first, second, and twentieth cycles in the voltage range of 3.75 V to 2.5 V are shown in Figures 9a and 9b for the batteries fabricated from P500 and P800 powders, respectively. Batteries were charged and discharged at 1 mA current. The deintercalation potentials (i.e. voltage of charge plateau) of the P500 and P800 compounds were equal to 2.94 V and 2.95 V with respect to Li anode potential. The voltages of the discharge plateaus were equal to 2.78 V and 2.82 V for the P500 and P800 batteries, respectively. The charge and discharge potential plateaus increased with calcination temperature. This might be attributed to the effect of calcination temperature on the formation of the spinel phase. The discharge-specific capacities of the batteries over 20 cycles are shown in Figure 10. It exhibits a significant fade of 15% of the initial capacity for the P500 batteries and an improvement of capacity of about 10% over cycling for the P800 batteries. The attainable capacities after 20 cycles are 83.4 mAh/g and 96.5 mAh/g for the P500 and P800 compounds, respectively. The effect of calcination temperature on the coulombic efficiency is obvious from Figure 10. The fact that the P500 compound exhibits a significant capacity fade over cycling may also

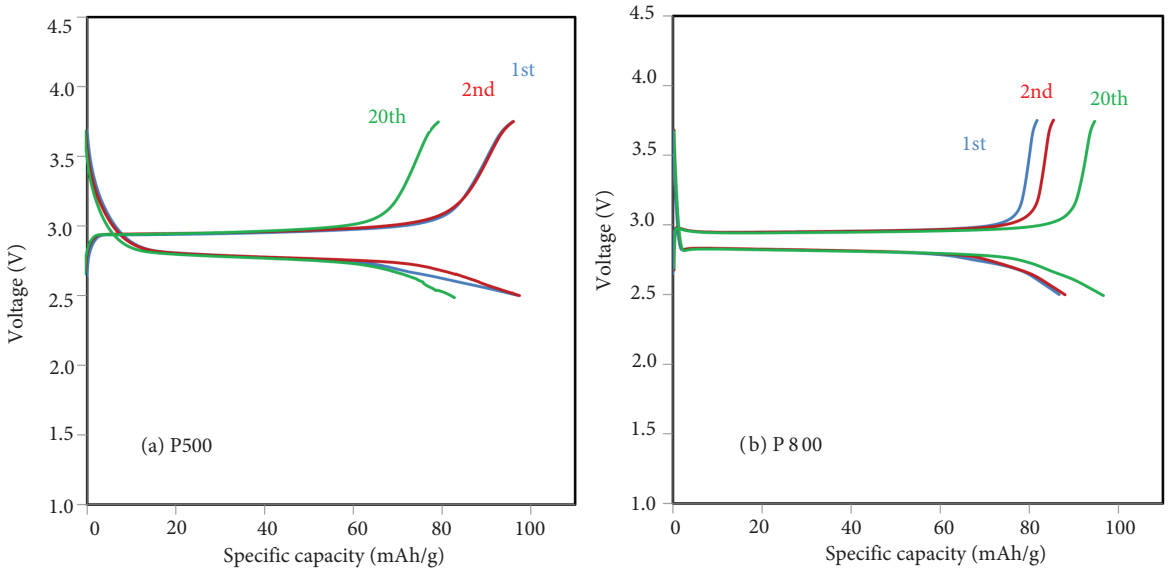

Figure 9. Galvanostatic charge and discharge curves of the first, second, and twentieth cycles of the batteries: (a) battery fabricated from P500 powder, (b) battery fabricated from P800 powder.

be understood based on analysis of the potential profile of Figure 8, where this material was found to undergo overlithiation at relatively lower voltages than the P800 compound. Overlithiation of the spinel structure is known to cause irreversible structural changes that finally lead to loss of capacity [25]. The dependence of specific capacity on discharge current for the P800 compound was investigated as shown in Figure 11, which exhibits a linear behaviour. The discharge capacity decreased from 94.6 mAh/g at 1 mA (i.e. current density of 40 mA/g) to 74 mAh/g at 2.5 mA (100 mA/g).

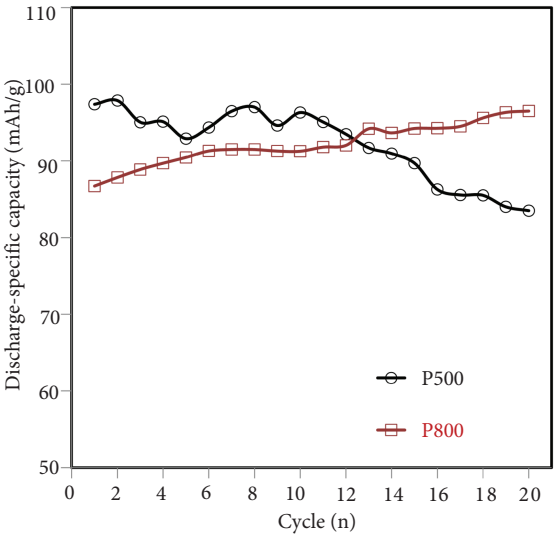

Figure 10. Discharge-specific capacities of the P500 and P800 batteries over 20 cycles.

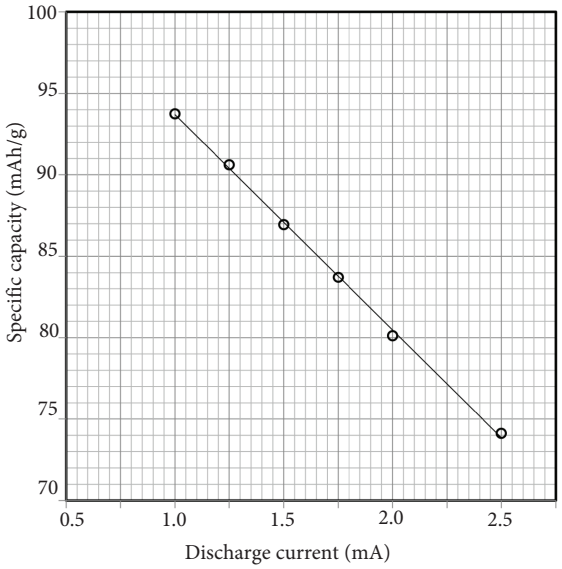

Figure 11. The dependence of specific capacity on discharge current for the P800 battery.

4. Conclusions

From the present analysis, a cathode compound of the form $Li_{1.03}Mn_{1.72}Ni_{0.16}Fe_{0.04}O_4$ was successfully synthesised for lithium rechargeable battery application. The lithium ion batteries, fabricated from the present powders, exhibited outstanding features of flat potential plateau and minimal voltage drop, emphasising a minimal capacitor-like behaviour. The effect of calcination temperature on battery performance was such that batteries prepared from powders calcined at 800 °C exhibited higher coulombic efficiency and better cycling performance than powders calcined at 500 °C. These features were attributed to elimination of the impurity phase and development of a single phase structure. The present material is thought to be a potential candidate for energy storage applications as a high-rate rechargeable battery.

Acknowledgment

One of the authors, AAA Al-Tabbakh, thanks the Universiti Teknologi MARA for support through a postdoctoral fellowship.

References

[1] Hosono, E.; Matsuda, H.; Honma, I.; Ichihara, M.; Zhou, H. *J. Electrochem. Soc.* **2007**, *154*, A146–A149.

[2] Ohzuku, T.; Ariyoshi, K.; Takeda, S.; Sakai, Y. *Electrochim. Acta* **2001**, *46*, 2327–2336.

[3] Feng, C.; Li, H.; Zhang, C.; Guo, Z.; Wu, H.; Tang, J. *Electrochim. Acta* **2012**, *61*, 87–93.

[4] Kim, B. H.; Choi, Y. K.; Choa, Y. H. *Solid State Ionics* **2003**, *158*, 281–285.

[5] Xiao, J.; Chen, X. L.; Sushko, P. V.; Sushko, M. L.; Kovarik, L.; Feng, J. J.; Deng, Z. Q.; Zheng, J. M.; Graff, G. L.; Nie, Z. et al. *Adv. Mater.* **2012**, *24*, 2109–2116.

[6] Arrebola, J. C.; Caballero, A.; Cruz, M.; Hernán, L.; Morales, J.; Castellón, E. R. *Adv. Funct. Mater.* **2006**, *16*, 1904–1912.

[7] Alcántara, R.; Jaraba, M.; Lavela, P.; Tirado, J. L. *Electrochim. Acta* **2002**, *47*, 1829–1835.

[8] Wang, X.; Nakamura, H.; Yoshio, M. *J. Power Sources* **2002**, *110*, 19–26.

[9] Liu, J.; Manthiram, A. *J. Phys. Chem.* **2009**, *C113*, 15073–15079.

[10] Aruna, S. T.; Mukasyan, A. S. *Curr. Opin. Solid State Mater. Sci.* **2008**, *12*, 44–50.

[11] Patil, K. C.; Aruna, S. T.; Mimani, T. *Curr. Opi. Solid State Mater. Sci.* **2002**, *6*, 507–512.

[12] Kamarulzaman, N.; Jaafar, M. H. *Stoichiometry and Materials Science – When Number Matters: Synthesis and Stoichiometric Analysis of a Li-Ion Battery Cathode Material*; InTech: Rijeka, Croatia, 2012.

[13] Lu, C. H.; Lin, S. W. *J. Power Sources* **2001**, *97*, 458–460.

[14] Stojanović, Z.; Marković, S. *Technics-New Materials* **2012**, *21*, 11–20.

[15] Orman, H. J.; Wiseman, P. J. *Acta Crystalogr.* **1984**, *C40*, 12–14.

[16] Guinebretiere, R. *X-Ray Diffraction by Polycrystalline Materials*; LSTE Ltd.: London, UK, 2007.

[17] Wolska, E.; Piszora, P.; Stempin, K.; Catlow, C. R. A. *J. Alloys. Compds.* **1999**, *286*, 203–207.

[18] Piszaora, P.; Catlow, C. R. A.; Woodley, S. M.; Wolska, E. *Comput. Chem.* 2000, *24*, 609–613.

[19] Pauling, L.; Shappell, M. D. *Z. Kristallogr.* **1930**, *75*, 128–142.

[20] Kawai, H.; Nagata, M.; Tukamoto, H.; West, A. R. *Electrochem. Solid State Lett.* **1998**, *1*, 212–214.

[21] Shokoohi, F. K.; Tarascon, J. M.; Wilken, B. J.; Guyomard, D.; Chang, C. C. *J. Electochem. Soc.* **1992**, *139*, 1845–1849.

[22] Sankpal, A. M.; Sawant, S. R.; Kakatkar, S. V.; Patil, R. S.; Chaudari, N. D.; Suryavanshi, S. S. *Proceedings of the International Conference on Computers and Devices for Communication*; Science City: Calcutta, India, 1998.

[23] Ghanbarnezhad, S.; Nemati, A.; Bavand-Vandchali, M.; Naghizadeh, R. *Int. J. Eng. Adv. Technol.* **2013**, *2*, 85–87.

[24] Yi, T. F.; Hao, C. L.; Yue, C. B.; Zhu, R. S.; Shu, J. *Synthetic Metals* **2009**, *159*, 1255–1260.

[25] Rana, J.; Glatthaar, S.; Gesswein, H.; Sharma, N.; Binder, J. R.; Chernikov, R.; Schumacher, G.; Banhart, J. *J. Power Sources* **2014**, *255*, 439–449.